Hydrodynamic fluctuations in confined emulsions

Nicolas Desreumaux,[1, *] Jean-Baptiste Caussin,[1, †] Raphael Jeanneret,[1, ‡] Eric Lauga,[2, §] and Denis Bartolo[1, 3, ¶]

[1]*Laboratoire de physique et mécanique des milieux hétérogènes, PMMH, ESPCI ParisTech,*
CNRS UMR 7636, Université Paris 6 et Université Paris 7, 10 rue Vauquelin, 75005 Paris, France.
[2]*Department of Mechanical and Aerospace Engineering,*
University of California San Diego, 9500 Gilman Drive, La Jolla CA 92093-0411, USA.
[3]*Laboratoire de Physique de l'Ecole Normale Supérieure de Lyon,*
Université de Lyon and CNRS, 46, allée d'Italie, F-69007 Lyon, France.
(Dated: January 24, 2013)

When an ensemble of particles interact hydrodynamically, they generically display large-scale transient structures such as swirls in sedimenting particles [1], or colloidal strings in sheared suspensions [2]. Understanding these nonequilibrium fluctuations is a very difficult problem, yet they are of great importance for a wide range of processes including pigment deposition in cosmetic or paint films, the transport of microfluidic droplets, ... All these samples concern rigidly confined fluids, which we consider in this paper. We address the collective dynamics of non-Brownian droplets cruising in a shallow microchannel. We provide a comprehensive characterization of their spatiotemporal density fluctuations. We show that density excitations freely propagate at all scales, and in all directions even though the particles are neither affected by potential forces nor by inertia. We introduce a theory which quantitatively accounts for our experimental findings. By doing so we demonstrate that the fluctuation spectrum of this nonequilibrium system is shaped by the combination of truly long-range hydrodynamic interactions and local collisions.

Understanding the collective dynamics of non-brownian particles in viscous fluids is a long-standing challenge in fluid mechanics. A typical example is the still unsolved problem of sedimentation in a quiescent fluid. Rather than falling along straight lines, as an isolated particle would do, sedimenting particles experience additional swirling motion correlated over large yet finite distances. The physical origin of those dynamical structures has been under debate for more than 30 years [3, 4]. The conceptual complexity of this collective dynamics contrasts with the formal simplicity of the (linear) Stokes equation that rules low-Reynolds-number flows. Immersed bodies generically affect both the momentum and the mass transfers of the fluid, even when not driven by external fields. As a result, long-range effective interactions arise between the particles due to the interplay between the local velocity of the fluid and the motion of the particles. The particle transport problem thus corresponds to a many-body dynamical system, that is intrinsically non-linear. The hydrodynamic interactions actually vanish only for uniform flow fields, for which the particles would be all advected at the same speed as the fluid, irrespective of their spatial distribution. Such a condition is never achieved when the fluid is rigidly confined. For instance, when particles are driven in thin channels or in (semi)rigid films, the momentum exchange with the bounding walls causes strong distortions of the flow field, thereby inducing effective interactions between the particles [5–8]. As it turns out, the transport of particle-ladden fluid in thin films is involved in a number of industrial and natural processes, including protein motion in lipid membranes [5], bacteria swarming [9, 10], colloid deposition on solid surfaces [11, 12], and droplet-based microfluidics [13]. Understanding the

particle transport in rigidly confined films is a first step toward the description of particle traffic in more complex geometries such as ordered, or random porous networks. The pioneering experiments by Rouyer et al. revealed
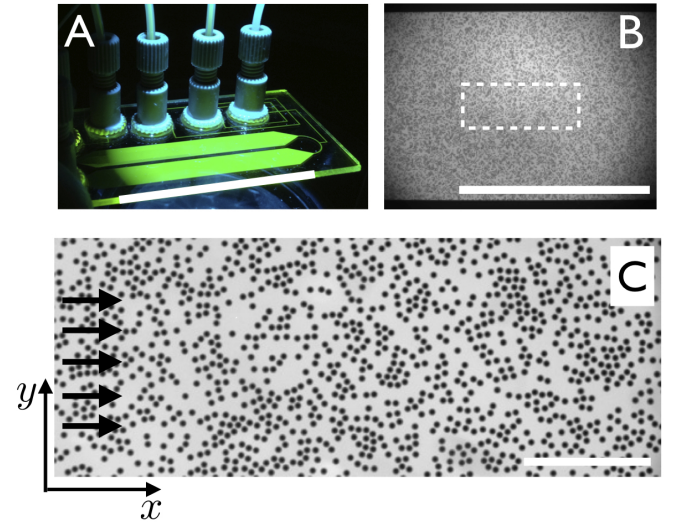

FIG. 1. A- Picture of the microfluidic setup. It is composed of: (i) a conventional flow-focusing junction, (ii) two dilution channels, and (iii) two identical wide observation channels. During the experiment one of these two 5-cm long channels is continuously fed with monodisperse droplets having a diameter comparable to the channel height. Scale bar: 5 cm. B- Close up on the main channel. Droplet diameter: $33.4\,\mu m$. Scale bar: 5 mm. C- Typical snapshot of a movie used to track the droplet positions. The field of view corresponds to the dashed rectangle in B. The black arrows indicate the direction of the flow. Scale bar: $500\,\mu m$.

that an ensemble of confined particles advected by a uniform viscous flow displays short-range structural correlations akin to the one found in simple liquids at the molecular scale [14]. More recently, Beatus and coworkers exploited a simple microfluidic experiment to probe the propagation of density heterogeneities in bidimensional emulsions [15]. They showed that the dynamic creation and destruction of droplet clusters also display a temporal coherence. Focusing on a semi-local quantity, the area fraction averaged over the channel width, they demonstrated that the droplet velocity is an increasing function of the local density, which is the elementary ingredient to give rise to Burgers (nonlinear) shock waves. The same phenomenology was also found in focused particle streams [16]. However, this elegant observation does not account for the complexity of the spatiotemporal fluctuations generically observed at all scales in rigidly confined particle-laden fluids.

Here we combine experimental and theoretical results to shed light on the collective dynamics of particles cruising through large-scale microfluidic channels. We first provide a comprehensive characterization of the density fluctuations observed in our experiments, and unveil their propagative nature at all scales, and in all directions. Then, we quantitatively demonstrate how the fluctuation spectrum of this many-body non-equilibrium system is shaped by the combination of truly long-range hydrodynamic interactions and local collisions.

EXPERIMENTAL RESULTS

Briefly, our experimental system consists of a monodisperse emulsion flowing in a shallow microchannel. The length and width of the channel, $L \times W = 5 \, \mathrm{cm} \times 5 \, \mathrm{mm}$, are much larger than its height, $h = 27 \pm 0.1 \, \mu\mathrm{m}$, which compares with the droplet diameter, see Fig. 1. The emulsion is therefore confined in a quasi-2D geometry. The droplets are formed at a conventional flow-focusing junction followed by a dilution module. The fluid flow-rates are imposed by high-precision syringe pumps. Etched-glass microchips ensure that the channel dimensions are unaffected by the flow conditions. In addition, the geometry of the junction, and the range of flow rates, are chosen so-that the formation of the droplet was unaffected by the dilution flow. By doing so, we accurately control both the droplet radius, R_d, and the average area fraction, ϕ, occupied by the emulsion. We report here results obtained for $R_d = 16.7 \pm 0.3 \, \mu\mathrm{m}$ ($R_d/h = 0.62$), and $0.21 < \phi < 0.56$. Varying the droplet sizes up to $R_\mathrm{d} \sim 2h$ does not qualitatively change our measurements. The droplets are visualized using fluorescence imaging. For each experiment we tracked $\sim 10^5$ particle trajectories in a region close to the center of the main channel, see Fig. 1B and 1C. More details about the microfluidic and the imaging setup are provided in the Materials and Methods section.

In the absence of droplets, the fluid flow would be uniform along the x-direction in the observation region. This is evidenced by the linear trajectories followed by isolated droplets cruising along the channel. Conversely, even at the smallest surface fraction, when an emulsion flows, the droplets undergo large transverse and longitudinal fluctuations in their motion, as shown in the supplementary movie (Video S1). These fluctuations lead to the formation of particle clusters at all scales. Interestingly, these clusters are clearly seen to travel at a speed that is different from the mean droplet velocity: transverse clusters are faster, whereas the longitudinal ones are slower. However, these clusters are transient structures, they form and break apart in a continuous fashion. Our purpose is to elucidate the physical mechanisms responsible for this complex and fluctuating dynamics. To quantify the spatiotemporal fluctuations of the droplet density field $\rho(\mathbf{r}, t)$, where $\mathbf{r} = (x, y)$, we measure its power spectrum, that is the dynamic structure factor. Introducing the Fourier transform of the local density: $\rho_{\mathbf{q},\omega'} = \frac{1}{2\pi} \int \rho(\mathbf{r}, t) e^{i(\mathbf{q}\cdot\mathbf{r} - \omega' t)} \mathrm{d}\mathbf{r} \, \mathrm{d}t$, the power spectrum is defined as $|\tilde{\rho}_{\mathbf{q},\omega'}|^2$, where $\tilde{\rho}(\mathbf{r}, t) \equiv \rho(\mathbf{r}, t) - \langle \rho(\mathbf{r}, t) \rangle$. Practically, ρ is computed from the particle positions as $\rho(\mathbf{r}, t) \equiv \sum_i \mathcal{G}(\mathbf{r} - \mathbf{r}_i(t))$, where $\mathbf{r}_i(t)$ is the position of the ith droplet, and where $\mathcal{G}$ is a Gaussian shape function of width $R_\mathrm{d}/15$, see Materials and Methods.

In Fig 2A, we show a slice of a typical power spectrum in the (ω', q_x) plane. This example corresponds to $\phi = 0.39$, and to $q_y R_\mathrm{d} = 0.2$. Several important comments are in order: (i) The power spectrum is localized in the Fourier space, which is the hallmark of propagative dynamics for the density fluctuations, as first noted in [15] for the specific case of the y-averaged density mode ($q_y = 0$). We stress that compression modes propagate even though the droplets do not interact via potential forces, and even though their inertia is negligible compared to the viscous friction at this scale. These "sound" modes originate only from the hydrodynamic coupling between the advected particles. (ii) The curve on which the spectrum is peaked corresponds to the dispersion curve of the density waves. We emphasize that it deviates markedly from a straight line at moderate wavelengths. The hydrodynamic interactions do not merely renormalize the mean advection speed and cause the density fluctuations to propagate in a dispersive fashion. (iii) The global shape of the spectrum is conserved for every area fraction, and more surprisingly for every wave vector q_y provided that the wavelength remains larger than the particle size (see below).

In all that follows, we discard the trivial non-dispersive contribution due to the advection at the mean droplet velocity $\langle \mathbf{v}_\mathrm{d} \rangle$. To do so, we focus on the density fluctuations in the frame moving at $\langle \mathbf{v}_\mathrm{d} \rangle$, and introduce the reduced pulsation $\omega \equiv \omega' - \langle v_\mathrm{d} \rangle q_x$. Experiments done at different area fractions, and thus at different continuous phase
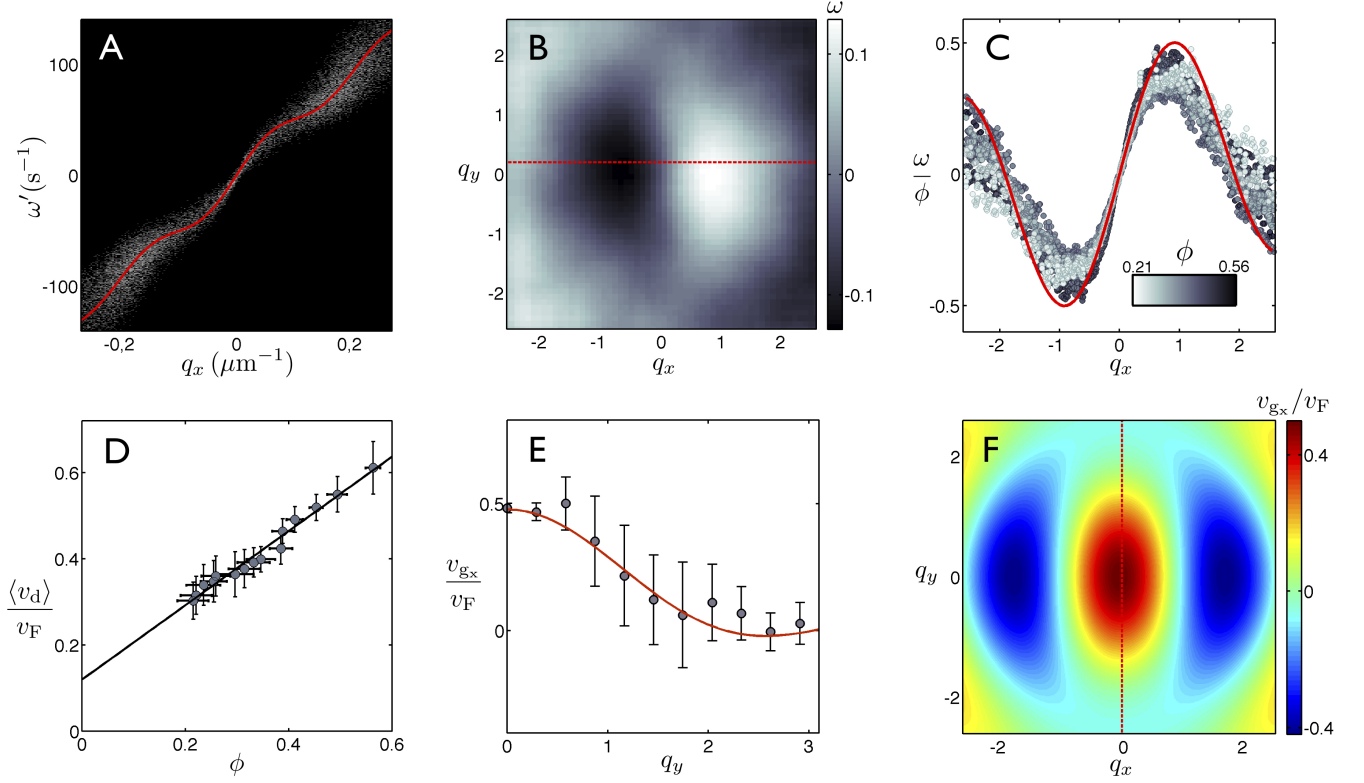
FIG. 2. A- Grayscale power spectrum of the density fluctuations plotted in the (q_x, ω') plane for $q_y = 0.2/R_d$. Area fraction $\phi = 0.39$, mean fluid velocity: $v_F = 1\,\mathrm{mm}/s$. Solid line: theoretical prediction for the location of the dispersion curve. B- Experimental dispersion curve in the frame moving at $\langle \mathbf{v}_d \rangle$, for $\phi = 0.39$. ω is plotted versus q_x, and q_y. We recall that units are chosen so that $R_d = 1$, and $v_F = 1$. The dotted line indicates the q_y value corresponding to the power spectrum shown in A. C- Renormalized dispersion relations in the moving frame, for $q_y = 0$. Circles: experimental data ($\phi = 0.21, 0.25, 0.30, 0.31, 0.33, 0.35, 0.38, 0.39, 0.41, 0.45, 0.49, 0.56$). Solid line: theoretical prediction, Eq. 8, with no adjustable parameter. D- Variations of the (rescaled) mean droplet velocity as a function of the area fraction. Circles: experimental data. Solid line: best linear fit. The error bars account for statistical fluctuations, and correspond to the standard deviation. E- v_{g_x} plotted versus q_y at $q_x = 0$. Circles: experimental data for $\phi = 0.56$. Solid line: Theoretical prediction with no adjustable parameter deduced from Eq. 8. The error bars correspond to a 95% confidence interval in the measurement of v_{g_x} from the slope of the dispersion curve. F- Theoretical prediction for the variations of the group velocity, v_{g_x} with the wave vector components. Dotted line: $q_x = 0$. The variations of v_{g_x} along this direction are shown in E.

velocities, are compared by normalizing the pulsations, and the wave vectors by v_F/R_d, and R_d^{-1} respectively. Fig 2B shows a typical dispersion relation: $\omega = \omega(q_x, q_y)$, obtained for $\phi = 0.39$. The spectrum is symmetric along the q_y direction as expected from the symmetry of the system. More importantly, density fluctuations propagate in all directions except in the one strictly transverse to the flow ($q_x = 0$). In addition, the dispersion curve displays an axial symmetry with respect to the q_y-axis. It is worth noting that the sign of the associated phase velocity changes as q_x increases. The long wavelength excitations propagate downstream, while the short wavelength excitations propagate upstream.

In Fig. 2C, we show that once renormalized by ϕ, the dispersion relations corresponding to 12 different area fractions collapse on a single master curve. This notice-able collapse is not specific to the purely longitudinal waves and occurs for all the possible q_y values. This systematic rescaling demonstrate that a unique set of physical mechanisms dictates the collective motion of the droplets, at all scales, regardless of the droplet density. We now establish a theoretical model which quantitatively accounts for these robust experimental findings.

THEORY AND DISCUSSION

We did not observe any deformation of the droplets in our experiments. Therefore, the instantaneous configuration of the emulsion is fully determined by the positions of N identical axisymmetric particles: $\mathbf{r}_i(t)$, $i = 1 \ldots N$. The dynamics of an isolated particle has proven to be

correctly captured by a constant mobility coefficient, μ, defined as $\dot{\mathbf{r}}_i(t) \equiv \mu\mathbf{v}(\mathbf{r}_i, t)$ where $\mathbf{v}(\mathbf{r}, t)$ is the in-plane fluid velocity field averaged over the channel height in the absence of the particle i [15]. In our quasi-2D geometry, the fluid flow is a potential flow and derives from the local pressure field: $\mathbf{v} = -G\nabla P$ where $G = h^2/12\,\eta$, η being the viscosity of the aqueous phase. $\mathbf{v}(\mathbf{r}, \mathbf{t})$ is then fully determined when considering the incompressibility condition, and the no-flux boundary conditions through the sidewalls of the channel as well. In a particle-free channel, the velocity field would be uniform, $\mathbf{v} = v_{\mathrm{F}}\hat{\mathbf{x}}$. The particles are not passive tracers ($\mu < 1$), therefore their relative motion with respect to the fluid results in a dipolar disturbance of the surrounding flow, as shown in [5, 6]. The potential dipolar perturbation, $\mathbf{v}^{\mathrm{dip}}(\mathbf{r}, \mathbf{r}_i(t))$, induced at the position $\mathbf{r}$ by a particle located at $\mathbf{r}_i(t)$ is defined by the modified incompressibility relation:

$$\nabla \cdot \mathbf{v}^{\mathrm{dip}}(\mathbf{r}, \mathbf{r}_i(t)) = \sigma \partial_x \delta(\mathbf{r} - \mathbf{r}_i(t)) \qquad (1)$$

where σ is the dipole strength ($\sigma > 0$). To establish the equations of motion of the N particles, we now assume the dipolar disturbances to be pairwise additive. This yields:

$$\dot{\mathbf{r}}_i(t) = \mu v_{\mathrm{F}}\hat{\mathbf{x}} + \mu \sum_{j \neq i} \mathbf{v}^{\mathrm{dip}}(\mathbf{r}_i(t), \mathbf{r}_j(t)) \qquad (2)$$

We now show how to move from these N coupled equations to an hydrodynamic description for the particle density field $\rho(\mathbf{r}, t)$. We follow a well established kinetic theory framework, see e.g. [17, 18]. We first introduce the N-point distribution function, $\rho^{(N)}(\mathbf{r}_1, ..., \mathbf{r}_N, t)$, to find particles at $\mathbf{r}_1, ..., \mathbf{r}_N$ at the time t. In a stationary state $\frac{\mathrm{d}}{\mathrm{d}t}\rho^{(N)} = 0$. We use this relation and Eq. 1 to derive the Fokker-Planck equation obeyed by $\rho^{(N)}$:

$$\partial_t \rho^{(N)} + \mu \sum_{i=1}^{N} \nabla_{\mathbf{r}_i} \cdot [v_{\mathrm{F}}\hat{\mathbf{x}}\rho^{(N)} \qquad (3)$$
$$+ \sum_{j \neq i} \mathbf{v}^{\mathrm{dip}}(\mathbf{r}_i(t), \mathbf{r}_j(t))\rho^{(N)}] = 0$$

We now exploit two assumptions: the hydrodynamic interactions are assumed to be pairwise additive, and the particles are all identical. Therefore we can establish a mass conservation equation that couples the local density $\rho(\mathbf{r}, t)$ to the two-point distribution function $\rho^{(2)}(\mathbf{r}, \mathbf{r}', t)$ only. It is obtained by integrating Eq. 3 over $N - 1$ particle positions;

$$\partial_t \rho(\mathbf{r}, t) + \mu v_{\mathrm{F}}\partial_x \rho(\mathbf{r}, t) \qquad (4)$$
$$+ \mu \nabla \cdot \int d\mathbf{r}' \mathbf{v}^{\mathrm{dip}}(\mathbf{r}, \mathbf{r}')\rho^{(2)}(\mathbf{r}, \mathbf{r}', t) = 0$$

where, $\rho(\mathbf{r}, t) \equiv \frac{1}{(N-1)!} \int \rho^{(N)}(\mathbf{r}, \mathbf{r}_2, ..., \mathbf{r}_N, t)\mathrm{d}\mathbf{r}_2 \ldots \mathrm{d}\mathbf{r}_N$, $\rho^{(2)}(\mathbf{r}, \mathbf{r}', t) \equiv \frac{1}{(N-2)!} \int \rho^{(N)}(\mathbf{r}, \mathbf{r}', \mathbf{r}_3, ..., \mathbf{r}_N, t)\mathrm{d}\mathbf{r}_3 \ldots \mathrm{d}\mathbf{r}_N$.

We now assume that the particle positions decorrelate over a distance as small as one particle diameter. In addition to this mean-field approximation, we also explicitly account for the steric repulsion between the particles. To do so, we postulate the following closure relation for Eq. 4:

$$\rho^{(2)}(\mathbf{r}, \mathbf{r}') = \left| \begin{array}{ll} 0 & \text{if } |\mathbf{r} - \mathbf{r}'| < 2R_{\mathrm{d}} \\ \rho(\mathbf{r})\rho(\mathbf{r}') & \text{if } |\mathbf{r} - \mathbf{r}'| \geq 2R_{\mathrm{d}} \end{array} \right. \qquad (5)$$

where R_{d} is the radius of a particle. Eqs. 4 and 5 define the equations of motion for the particle-density field. In principle, the effective extent of the excluded volume could be larger that the particle radius due to short-range intermolecular repulsions, and lubrication forces. However no measurable difference with the actual droplet radius could be observed in our experiments.

We now focus on the dynamics of small density fluctuations, $\tilde{\rho}(\mathbf{r}, t)$, around an homogeneous state: $\tilde{\rho}(\mathbf{r}, t) \equiv \rho(\mathbf{r}, t) - \rho_0$, where $\rho_0 = \langle\rho(\mathbf{r}, t)\rangle = \phi/(\pi R_{\mathrm{d}}^2)$. As done in our experiments, we work in the frame moving at the mean droplet velocity $\langle\mathbf{v}_{\mathrm{d}}\rangle = \mu v_{\mathrm{F}}\hat{\mathbf{x}} + \mu\rho_0 \int_{|\mathbf{r}-\mathbf{r}'|\geq 2R_d} \mathbf{v}^{\mathrm{dip}}(\mathbf{r}, \mathbf{r}') \mathrm{d}\mathbf{r}'$. At leading order in $\tilde{\rho}$, Eqs. 4 and 5 then reduce to:

$$\partial_t \tilde{\rho}(\mathbf{r}, t) + \nabla \cdot \tilde{\mathbf{j}}(\mathbf{r}, t) = 0 \qquad (6)$$

where both the hydrodynamic interactions (long-range) and the contact interactions (short-range) are captured by the current functional $\tilde{\mathbf{j}}(\mathbf{r}, t) \equiv \mu\rho_0 \int_{|\mathbf{r}-\mathbf{r}'|\geq 2R_d} \mathbf{v}^{\mathrm{dip}}(\mathbf{r}, \mathbf{r}')\tilde{\rho}(\mathbf{r}', t) \mathrm{d}\mathbf{r}'$. Using Eq. 1 and focusing on particles far from the sidewalls, we can show that $\nabla \cdot \tilde{\mathbf{j}}$ is actually a local quantity:

$$\nabla \cdot \tilde{\mathbf{j}}(\mathbf{r}, t) = -\frac{\mu\rho_0\sigma}{4\pi R_{\mathrm{d}}} \int \tilde{\rho}(\mathbf{r} - 2R_{\mathrm{d}}\hat{\mathbf{r}}')\cos\theta' \mathrm{d}\theta' \qquad (7)$$

Since $R_{\mathrm{d}} \ll W$ we have used the expression of the dipolar perturbation corresponding to an unbounded domain: $\mathbf{v}^{\mathrm{dip}}(\mathbf{r}, \mathbf{r} + 2R_{\mathrm{d}}\hat{\mathbf{r}}') \cdot \hat{\mathbf{r}}' = -(\sigma\cos\theta')/8\pi R_{\mathrm{d}}^2$, where $\hat{\mathbf{r}}' \equiv \cos\theta'\hat{\mathbf{x}} + \sin\theta'\hat{\mathbf{y}}$ [6]. We now look for plane wave solutions $\tilde{\rho}(\mathbf{r}, t) = \sum_{\mathbf{q}} \tilde{\rho}_{\mathbf{q}}\exp(i\omega t - i\mathbf{q}\cdot\mathbf{r})$ of Eq. 6. After some elementary algebra we infer their dispersion relation, which is our main theoretical result:

$$\omega = (\mu\sigma\rho_0)q_x \frac{J_1(2qR_{\mathrm{d}})}{2qR_{\mathrm{d}}} \qquad (8)$$

where J_1 is the first Bessel function. As ω is a real quantity, the above equation implies that density waves freely propagate in the channel in qualitative agreement with our experimental observations. It is worth noting that since $\nabla\cdot\tilde{\mathbf{j}}$ is a local quantity, the form of the dispersion relation is generic, and does not depend on the channel size, and geometry. In addition, we point that ω scales as ρ_0, which explains the collapse of the normalized dispersion relations on a single master curve over the entire range of wave vectors, Figure 2C. We now move to a quantitative

comparison between our theoretical prediction and our experimental measurements. Eq. 8 is fully determined by two physical parameters: the droplet radius R_d, and $\mu\sigma\rho_0$ that quantifies the strength of the hydrodynamic couplings. To determine this latter parameter, we exploit another specific feature of the long-range hydrodynamic interactions. In an isotropic and homogeneous system, due to their dipolar symmetry, the sum of all the hydrodynamic interactions would leave the mean droplet velocity unchanged. However, in anisotropic channel geometries, $\langle \mathbf{v}_d \rangle$ increases linearly with the mean density irrespective of the channel size [19]. At 0th order in $\tilde{\rho}$, $\langle \mathbf{v}_d \rangle = \mu v_F \hat{\mathbf{x}} + \frac{1}{2}(\mu\sigma\rho_0)\hat{\mathbf{x}}$. Importantly this relation provides a direct means to measure independently the last unknown parameter of our theory. Figure 2D clearly shows that the measured mean droplet speed increases with ρ_0 in an affine manner. The strength of the hydrodynamic coupling ($\mu\sigma\rho_0$) is readily infered from a linear fit, Figure 2D. We superimposed our theoretical predictions for the dispersion relation, Eq. 8, both in the laboratory frame and in the frame moving at $\langle \mathbf{v}_d \rangle$ in Figures 2A and 2C. We find that the agreement between the theory and the experiments is excellent over a wide range of wave vectors, and of area fractions. Without any free fitting parameters, our model quantitatively captures the dispersive nature of the density fluctuations observed in the flowing emulsions.

To gain more physical insight into the propagation of the density waves, it is worth looking at the small-q expansion of Eq. 8: $\omega = \frac{1}{2}\mu\sigma\rho_0 q_x [1 - \frac{1}{2}(qR_d)^2] + \mathcal{O}\left((qR_d)^4\right)$. At leading order, this relation is non-dispersive (linear) whatever the direction of propagation. The phase velocity scales linearly with the magnitude of the dipolar coupling σ. In addition, it does not depend explicitly on R_d, which implies that the small-q excitations propagate only due to the long-range hydrodynamic interactions between the particles. Conversely, the dispersive term in $\omega(\mathbf{q})$ explicitly depends on the particle radius. At high q, the propagation of the density waves is set by the combination of the excluded volume interactions and the angular symmetry of the hydrodynamic couplings.

We close this section by recalling that one of the most striking feature observed in the flowing emulsions is the propagation of vertical density bands which propagate significantly faster than the mean droplet flow, see supplemental material (Video S1). An homogeneous vertical band spanning the entire width of the channel corresponds to the linear superposition of plane waves associated with $q_y = 0$, and with q_xs distributed around $q_x = 0$. In the frame moving at $\langle \mathbf{v}_d \rangle$, their speed is given by the x-component of the group velocity $v_{g_x}(q_x, q_y) = \partial\omega/\partial q_x$ evaluated at $q = 0$. In Figure 2E, we plot the experimental values of $v_{g_x}(0, q_y)$, which we measured from the slope at the origin of the dispersion curves (as the ones shown in Figure 2C). Again the agreement with the theoretical curve deduced from Eq. 8 is excellent. This plot

reveals that the density bands extended across the entire channel width are the fastest and propagate at velocities 1.5 higher that the mean droplet flow, thereby making them highly visible on the experimental movies.

To go beyond this observation, we use Eq. 8, to plot the magnitude of $v_{g_x}(q_x, q_y)$ for all qs, see Fig. 2F. v_{g_x} displays non-monotonic variations with both q_x, and q_y and changes its sign at high qs. In the frame moving at $\langle \mathbf{v}_d \rangle$, and for $qR_d \ll 1$, v_{g_x} is positive. The wave packets propagate faster than the mean flow due to the hydrodynamic interactions that shape the dispersion curve in the long-wavelength limit. In contrast, the short-ranged "collisions" between the droplets result in the opposite effect: at high q the density-wave packets propagate upstream ($v_{g_x} < 0$, for $qR_d > 1$).

CONCLUSION

In conclusion, we shed light on the spatiotemporal fluctuations generically observed in flow-driven confined suspensions. We devised a model microfluidic experiment which made it possible to track the individual positions of hundred of thousands of identical droplets, interacting hydrodynamically, in a shallow channel. We demonstrated that density fluctuations freely propagate at all scales and along all directions in the channel, irrespective of the area fraction occupied by the droplets. Introducing a kinetic theory we elucidated the two physical ingredients that shape the dispersion curve of the linear excitations. At long wavelengths, non-dispersive sound modes propagate as a result of the dipolar hydrodynamic interactions caused by the motion of the confined droplets. Conversely, for wavelengths smaller than ten particle diameters the strongly dispersive nature of the density waves stems from the combination of both the excluded volume interactions and the hydrodynamic coupling. A challenging perspective to this study would be to consider the case of self-driven particle such as rigidly confined motile cells, and chemically propelled colloids and droplets which also display intriguing coherent structures at all scales [9, 21, 22].

MATERIALS AND METHODS

Microfluidics and image acquisition
The microfluidic device is a double etched fused silica/quartz custom-design chip (Micronit Microfluidics). It consists of a conventional flow-focusing junction followed by a dilution module and a large channel. We

used deionized distilled water with 0.1% SDS surfactant and fluorescein for the dispersed phase, and hexadecane (Sigma-Aldrich) for the continuous phase. The channel surface were cleaned in a UV/Ozone cleaner prior to the experiments, thereby making the glass surface highly hydrophilic. The injection into the channels is controlled by high-precision syringe pumps (Nemesys low pressure dosing modules, Cetoni). The device was mounted on a Nikon AZ100 upright macroscope. A Basler Aviator av2300-25gm (4 Megapixel, 8bit) camera was used to record the movement of the droplets in a field of view of 2.70mm $\times$ 1.03mm at the center of the channel. The frame rate was set at 45Hz.

Data analysis

From our movies, we detected the positions of the droplets to sub-pixel accuracy using a built in routine in the image processing program ImageJ. The particle velocities were then computed using the Matlab version of the tracking software developed by David Grier, John C. Crocker and Eric R. Weeks [20]. We used a custom Matlab routine to compute the power spectrum of the density fluctuations. First, we computed analytically the spatial Fourier transform of the density field at all time, using a Gaussian shape function of width $R_d/15$ (see main text), which typically corresponds to the precision on the particle position detection. Then, the temporal Fourier transform was computed numerically. To obtain the dispersion relations curves, we detected for each pulsation, ω, the wave-vector corresponding to the maximum of the power spectrum at this given pulsation.

———————

* nicolas.desreumaux@espci.fr
† jeanbaptiste.caussin@ens-lyon.fr
‡ raphael.jeanneret@espci.fr
§ elauga@ucsd.edu
¶ denis.bartolo@ens-lyon.fr

[1] P.N. Segrè, E. Herbolzheimer, and P. M.Chaikin, *Long-Range Correlations in Sedimentation*, Phys. Rev. Lett., 79, 2574 (1997).

[2] X. Cheng, X. Xu, S. A. Rice, A. R. Dinner, and I. Cohen, *Assembly of vorticity-aligned hard-sphere colloidal strings in a simple shear flow*, Proc. Natl. Acad. Sci. U.S.A.,109, 63 (2012).

[3] E. Guazzelli, and J. Hinch, *Fluctuations and Instability in Sedimentation*, Annual review of fluid mechanics, 43, 97 (2011).

[4] S. Ramaswamy, *Issues in the statistical mechanics of steady sedimentation*, Adv. Phys. 50, 297 (2001).

[5] E. Evans and E. Sackmann, *Translational and rotational drag coefficients for a disk moving in a liquid membrane associated with a rigid substrate*, J. Fluid Mech. 194, 553 (1988).

[6] B. X. Cui, H. Diamant, B.H. Lin, and S. A. Rice, *Anomalous hydrodynamic interaction in a quasi-two-dimensional suspension*, Phys. Rev. Lett. 92, 92.258301 (2004).

[7] J. Blawzdziewicz and E. Wajnryb, *An analysis of the far-field response to external forcing of a suspension in the Stokes flow in a parallel-wall channel*, Physics of Fluids, 20, 093303 (2008).

[8] R. Di Leonardo, E. Cammarota, G. Bolognesi, H. Schaefer, and M. Steinhart,*Three-Dimensional to Two-Dimensional Crossover in the Hydrodynamic Interactions between Micron-Scale Rods*, Physical Review Letters, 107, 20740-3844 (2011).

[9] H. P. Zhang, A. Beer, E.-L. Florin, and H. L. Swinney, *Collective motion and density fluctuations in bacterial colonies*, Proc. Natl. Acad. Sci. U.S.A. , 107(31), 1362630 (2010).

[10] R. Zhang, L. Turner, and H. C. Berg, *The upper surface of an Escherichia coli swarm is stationary*, Proc. Natl. Acad. Sci. U.S.A. , 107(1), 28890 (2010).

[11] R. D. Deegan, O. Bakajin, T. F. Dupont, G. Huber, S. R. Nagel, and T. A. Witten, *Capillary flow as the cause of ring stains from dried liquid drops*, Nature 389, 827-829 (1997).

[12] R. D. Deegan, O. Bakajin, T. F. Dupont, G. Huber, S. R. Nagel, and T. A. Witten, *Contact line deposits in an evaporating drop*, Physical Review. E 62, 75665 (2000).

[13] R. Seemann, M. Brinkmann, T. Pfohl, and S. Herminghaus, *Droplet based microfluidics*, Rep. Prog. Phys. 75, 016601(2012).

[14] F. Rouyer, D. Lhuillier, J. Martin, and D. Salin, *Structure, density, and velocity fluctuations in quasi-two-dimensional non-Brownian suspensions of spheres*, Phys. Fluids 12, 958 (2000).

[15] T. Beatus, T. Tlusty, and R. Bar-Ziv, *Burgers shock waves and sound in a 2D microfluidic droplets ensemble*, Phys. Rev. Lett. 103, 114502 (2009).

[16] N. Champagne, R. Vasseur, A. Montourcy, and D. Bartolo, *Traffic jams and intermittent flows in microfluidic networks*, Phys. Rev. Lett. 105, 044502 (2010).

[17] H. Risken, *The Fokker-Planck Equation: Methods of Solution and Applications*, Springer Verlag, Berlin (1996).

[18] A.M. Menzel, *Collective motion of binary self-propelled particle mixtures*, Phys. Rev. E 85, 021912 (2012).

[19] T. Beatus, R. Bar-Ziv, and T. Tlusty, *The physics of 2D microfluidic droplet ensembles*, Physics Reports, 516(3), 103-145 (2012).

[20] J.C. Crocker, and D.G. Grier, *Methods of digital video microscopy for colloidal studies*, J. Colloid Interface Sci. 179, 298 310 (1996).

[21] S. Thutupalli, R. Seemann, and S. Herminghaus, *Swarming behavior of simple model squirmers*, New J. Phys. 13, 073021 (2011).

[22] S. J. Ebbens, and J. R. Howse, *In pursuit of propulsion at the nanoscale*, Soft Matter 6, 726-738 (2010).